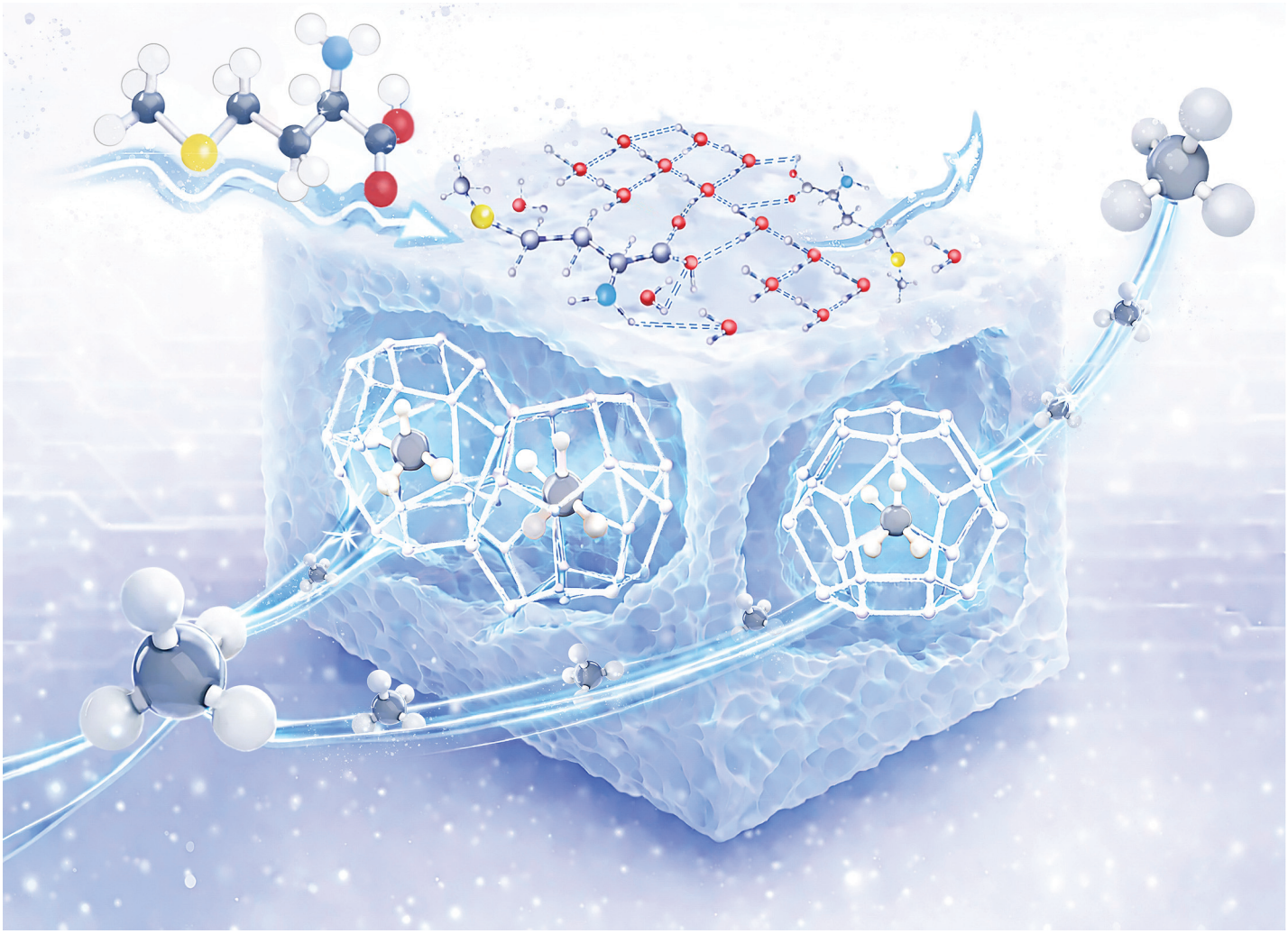

Showcasing research from Professor Zhenyuan Yin's Natural Gas Hydrate and Carbon Storage laboratory from Tsinghua University, China.

L-Methionine modified active ice enables ultra-rapid methane hydrate kinetics for solidified natural gas storage

Hydrate-based natural gas storage represents a novel energy carrier solution distinguished by its inherent safety and environmental sustainability. Diverging from traditional use of promoters in the aqueous phase, we introduce a hydrophobic amino acid L-methionine to engineer "active ice", that enables ultra-rapid CH_4 hydrate kinetics at the solid-gas interface within few minutes. We reveal that active ice possesses a unique porous structure with a partially ordered hydrogen-bonding network, providing a critical kinetics enhancement pathway to facilitate large-scale commercial adoption.

Image reproduced by permission of Zhenyuan Yin from *Green Chem.*, 2026, **28**, 5226.

As featured in:

See Zhenyuan Yin *et al.*, *Green Chem.*, 2026, **28**, 5226.

ROYAL SOCIETY OF CHEMISTRY

rsc.li/greenchem

Registered charity number: 207890

Green Chemistry

PAPER

View Article Online
View Journal | View Issue

Cite this: *Green Chem.*, 2026, **28**, 5226

L-Methionine modified active ice enables ultra-rapid methane hydrate kinetics for solidified natural gas storage

Yang Li, [a] Jibao Zhang, [a] Jingbo Gao, [a] Guangjin Chen[b] and Zhenyuan Yin *[a]

Hydrate-based solidified natural gas (SNG) technology offers significant potential due to its high volumetric density and inherent safety. However, the slow kinetics of CH_4 hydrate formation from conventional gas–liquid systems has long limited its large-scale application. Herein, we report a green approach by introducing an environmentally benign amino acid, L-methionine (L-Met), to synthesize active ice for ultra-rapid CH_4 hydrate kinetics. Active ice modified by optimal 0.3 wt% L-Met enabled a high CH_4 uptake of 156.05 V_g/V_w and a record-high growth rate with a t_{90} of 3.33 min, representing one of the fastest CH_4 hydrate formation rates to date. Cryogenic scanning electron microscopy revealed that 0.3 wt% L-Met modified active ice exhibited a well-connected porous structure with open pore size ranging from 7 to 17 μm, whereas both pure ice and high-dose L-Met modified active ice both exhibited a compact morphology with closed pores. We employ both *in situ* Raman and Fourier transform infrared spectroscopy to examine the micro-kinetics and reveal for the first time the strong correlation between ultra-rapid CH_4 hydrate kinetics and the partially ordered hydrogen bond network in active ice. High-dose L-Met modified active ice reduced the hydrogen bond ordering, while pure ice increased the rigidity of the ordered hydrogen bond. The combination of the designed partially ordered hydrogen bond network and the observed porous structure of the active ice collectively promoted the ultra-rapid formation of CH_4 hydrate for effective natural gas storage. Our study provides molecular-level insights into the mechanism of L-Met modified active ice in promoting CH_4 hydrate formation and develops an energy-efficient route for SNG technology.

Received 20th November 2025,
Accepted 26th January 2026

DOI: 10.1039/d5gc06216k

rsc.li/greenchem

Green foundation

1. We introduce an environmentally benign amino acid, L-methionine, to synthesize active ice that significantly enhances CH_4 hydrate kinetics and final CH_4 uptake. Using only water as the hydrate-former and low dose L-Met as the green promoter achieves effective and record-high CH_4 storage. The method avoids the environmental concerns associated with traditional surfactant-based promoters.
2. The optimal active ice enabled ultra-rapid CH_4 hydrate formation kinetics with a final CH_4 uptake of 156.05 ± 3.28 V_g/V_w and a t_{90} of 3.33 ± 0.43 min. This corresponds to a nearly 90-fold enhancement in gas uptake rate over conventional solution-based systems.
3. Future work will develop a series of hydrophobic amino acids for active ice synthesis based on the elucidated micro kinetics and mechanisms. A continuous production process will be developed for large-scale solidified natural gas storage application using the active ice method.

1. Introduction

The urgent need to mitigate carbon emissions and ensure energy security has accelerated the transition toward cleaner fuels.[1,2] As nations pursue carbon neutrality under the Paris Agreement, identifying efficient low-carbon energy carriers has become a central challenge in the sustainable energy landscape.[3,4] Natural gas (NG, predominantly CH_4) serves as a key transitional fuel due to its high energy efficiency and lower carbon emissions than other fossil fuels.[5] Realizing its potential, however, requires safe and efficient large-scale storage and transport technologies. Conventional approaches, such as liquefied natural gas (LNG), compressed natural gas (CNG), and adsorbed natural gas (ANG), face inherent limits. LNG offers high energy density but requires cryogenic temperatures (−162 °C), which increases energy and infrastructure costs.[6,7] CNG works at ambient temperature but requires high press-

[a]*Institute for Ocean Engineering, Shenzhen International Graduate School, Tsinghua University, Shenzhen, 518055, China. E-mail: zyyin@sz.tsinghua.edu.cn*
[b]*State Key Laboratory of Heavy Oil Processing, China University of Petroleum, Beijing, 102249, China*

ures (20–25 MPa), posing safety concerns.[8,9] ANG, using porous adsorbents such as activated carbon (AC)[10] or metal–organic frameworks (MOFs),[11] improves safety but involves high costs for material synthesis and shows poor recycling stability.

Hydrate-based solidified natural gas storage (SNG) technology offers a promising alternative.[12,13] Gas hydrates are crystalline compounds, typically formed under relatively high pressures (2–6 MPa) and low temperatures (0–10 °C). The guest gas molecules are encapsulated within hydrogen-bonded water cages. This structure enables a high volumetric storage density of approximately 170 m^3 of CH_4 gas in 1 m^3 of CH_4 hydrate under standard conditions.[14] Using water as the primary medium, SNG combines intrinsic safety, low cost, and environmental compatibility, while avoiding the high pressures and cryogenic requirements of conventional methods.[15,16] Moreover, gas hydrate formation and dissociation are fully reversible, allowing cyclic storage and release of gas with minimal energy penalty.[17] With these advantages, SNG is regarded as a sustainable pathway for medium-scale gas storage in rural areas without gas pipelines, offshore platforms and boil-off gas management. It bridges the gap between energy efficiency and environmental sustainability, positioning itself as a key technology for next-generation natural gas storage and transportation.

However, the large-scale application of SNG technology remains limited by the slow growth rate of CH_4 hydrate under practical conditions. To accelerate the formation kinetics, various strategies have been developed, including reactor design optimization,[18] incorporation of porous media,[19] and the use of kinetic promoters such as surfactants and amino acids.[20] Among these approaches, the addition of kinetic hydrate promoters is the simplest and most effective method to enhance CH_4 hydrate formation.[21,22] Among them, environmentally friendly amino acids such as L-methionine (L-Met) have been widely employed to enhance CH_4 hydrate formation kinetics. However, these solution-based systems typically suffer from both long induction times of tens of minutes[23,24] and prolonged growth periods extending to several hours, posing significant challenges for industrial scale-up.[25,26]

To overcome the kinetic barriers, the method of active ice modified by kinetic promoters was proposed. Xiao *et al.* first demonstrated the use of sodium dodecyl sulfate (SDS) to modify active ice, which achieves a high CH_4 uptake of 185.0 V_g/V_w with a t_{90} of 5.0 min.[27] However, SDS possesses environmental toxicity and is prone to generating foam during CH_4 hydrate dissociation, which is not ideal for large-scale applications.[26] Alternatively, amino acid L-tryptophan modified active ice has recently been employed to achieve a slightly lower CH_4 gas uptake of 146.6 V_g/V_w and rapid kinetics with a t_{90} of 2.4 min. However, the synthesis of active ice involves complex energy-intensive procedures, including stringent low-temperature freezing to 243.2 K and mechanical grinding.[28] Additionally, both studies only focused on the macroscopic rapid kinetics achieved by using the active ice method but did not fully examine the micro-kinetics of the process and elucidate the underlying promotion mechanism at the molecular level.

Herein, we introduce an environmentally benign hydrophobic amino acid, L-Met, as a new kinetic promoter to synthesize active ice by dissociating preformed CH_4 hydrate at a temperature close to the ice point (272.7 K). The L-Met modified active ice (hereafter referred as "active ice") exhibited outstanding performance in promoting CH_4 hydrate formation kinetics, achieving both an ultra-rapid formation rate and high CH_4 storage capacity. Furthermore, we elucidated how L-Met concentration regulated the pore structure of the active ice and the spatial distribution of L-Met on the ice surface using cryo-scanning electron microscopy (Cryo-SEM) with energy dispersive spectroscopy (EDS), as well as the hydrogen bond ordering in the active ice using both *in situ* Raman spectroscopy and Fourier transform infrared (FT-IR) spectroscopy. Experimental results pinpoint that both the partially ordered hydrogen network and the porous structure in active ice facilitate the ultra-rapid CH_4 hydrate formation kinetics. Our findings provide a sustainable and scalable solution for advancing green and effective SNG technology.

2. Experimental section

2.1. Materials

High-purity methane (CH_4, 99.9%) was supplied by Shenzhen Huatepeng Special Gas Co., Ltd. L-Methionine (L-Met, 99.9%) was sourced from Shanghai Aladdin Bio-Chem Technology Co., Ltd. Ultra-pure water, produced in-house, was used in all experiments.

2.2. Experimental apparatus

A schematic diagram of the experimental setup is shown in Fig. 1a. Briefly, it consists of a CH_4 gas cylinder (GC), a gas storage tank (GST), a circulating chiller (CC), a water bath (WB) with a magnetic stirrer (MS) at the bottom, a fully visualized reactor, a Charge-Coupled Device (CCD) camera, a data acquisition device, and a computer. The fully visualized reactor, constructed using 316 stainless steel and a sapphire column (see Fig. 1b), was employed for kinetic and morphological experiments. The height of the reactor was 150 mm with an internal diameter of 51 mm, providing an effective volume of 254.6 mL, with a maximum design pressure of 20.0 MPa.

A high-precision CCD camera (MAGELLAN, DJ630) recorded the side-view images of CH_4 hydrate morphology during the formation and dissociation processes. The gas storage tank (GST) served as a high-pressure reservoir for the CH_4 gas supply during the CH_4 hydrate formation experiment. Constructed using 316 stainless steel, this cylindrical vessel features a height of 600 mm and an outer diameter of 200 mm, with a wall thickness of 10 mm ensuring structural integrity under high-pressure conditions. The GST operates at a maximum working pressure of 20 MPa, regulated through precision needle valves (NVs) and monitored using an integrated pressure sensor (PS). To promote rapid CH_4 hydrate for-

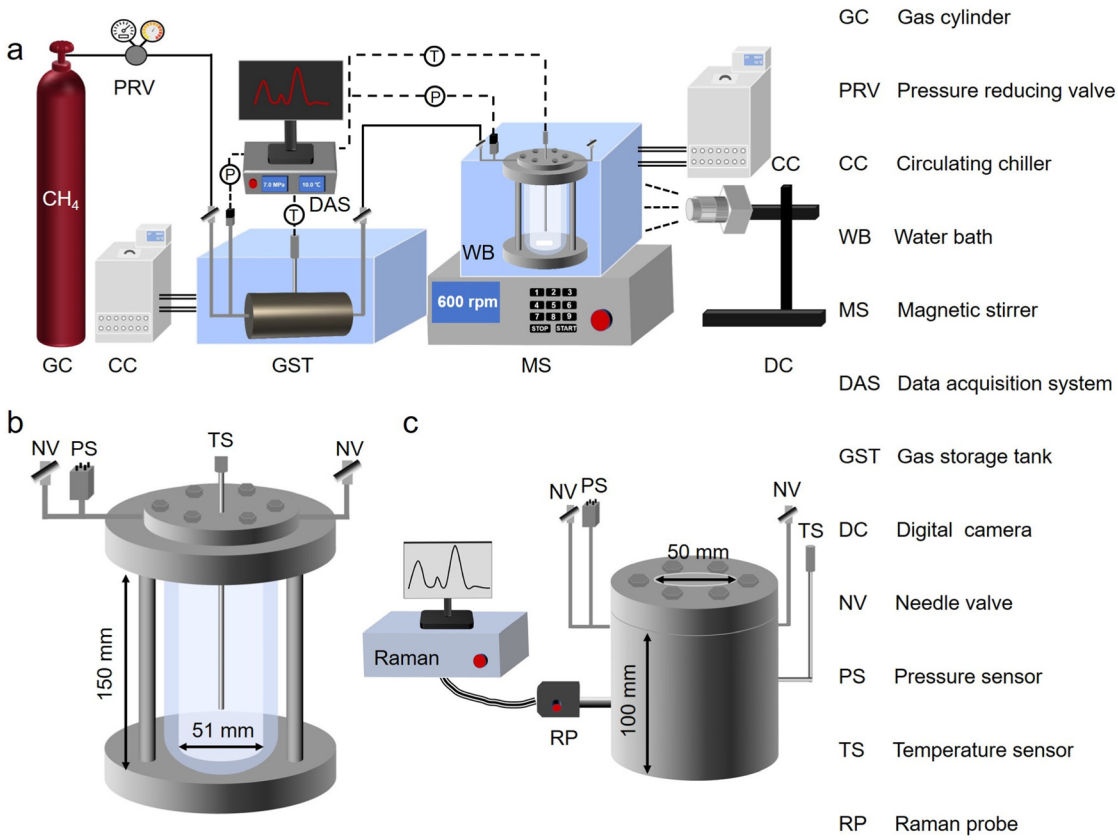

Fig. 1 (a) Schematic diagram of the experimental setup for the synthesis of L-Met modified active ice and CH_4 hydrate formation kinetic experiments, (b) the full-visualized reactor used for CH_4 hydrate kinetic and morphological observation, and (c) the non-visualized reactor integrated with the *in situ* Raman characterization.

mation from the L-Met solution, a magnetic stirrer was installed at the bottom of the transparent water bath. This arrangement ensured effective agitation of the liquid phase, promoting efficient gas–liquid interaction and enhancing CH_4 hydrate formation. A pressure sensor (Senex, DG2113-C-20, 0–20.0 MPa, accuracy ± 20 kPa) and a temperature sensor (Westzh, WZP-191, accuracy ± 0.1 K) were used for real-time monitoring of pressure and temperature, with data recorded every 5 s *via* a DAQ system. Cryogenic scanning electron microscopy (Cryo-SEM) with energy-dispersive X-ray spectroscopy (EDS) was first employed to examine the microstructure and surface elemental distribution of the synthesized active ice. The field emission SEM, equipped with an *in situ* cryogenic stage, provided high-resolution secondary electron (0.9 nm at 15 kV) and backscattered electron imaging (2.0 nm at 30 kV). The 100 mm^2 EDS detector allowed mapping of the presence of amino acid in active ice.

Additionally, a non-visualised reactor with an internal diameter of 50 mm and a height of 100 mm was employed, providing an effective volume of approximately 196.3 mL and capable of withstanding pressures up to 30.0 MPa. This reactor was primarily designed for *in situ* Raman measurement. A Raman probe (RP) was positioned at the side of this reactor. The exact locations are illustrated in Fig. S1. It was coupled with a Raman spectrometer (W2 Innovations) to enable *in situ* and time-dependent analysis of the formation and dissociation of CH_4 hydrate (see Fig. 1c). A high-pressure Raman probe with a diameter of 9.5 mm was mounted at the side of this reactor. The Raman probe was linked to the spectrometer *via* two optical fibres: one fibre transmitted the laser (532 nm, 100.0 mW) into the reactor, while the other transmitted the collected Raman signal. Raman spectroscopy was recorded over the 150–4490 cm^{-1} range with an integration time of 1.0 s during the experiment. The spectroscopy resolution was 2.8 cm^{-1} per pixel at 2000 cm^{-1}, achieved using a grating with 1800 grooves. Fourier transform infrared (FT-IR) spectroscopy (Nicolet, IS50) was used to characterize the hydrogen bond networks in the L-Met solution and active ice. The spectra were recorded in the range of 400–4000 cm^{-1} at a resolution of 1.2 cm^{-1}. For each spectrum, 32 scans were co-added to improve the signal-to-noise ratio.

2.3. Experimental procedure

The experimental procedure comprised three distinct stages:

(I) Initial CH_4 hydrate formation from L-Met solution (see Fig. 2a–e): the reactor was cleaned with deionized water and dried with air. Next, 40 mL of the prepared solution was injected into the reactor, which was then sealed and placed in

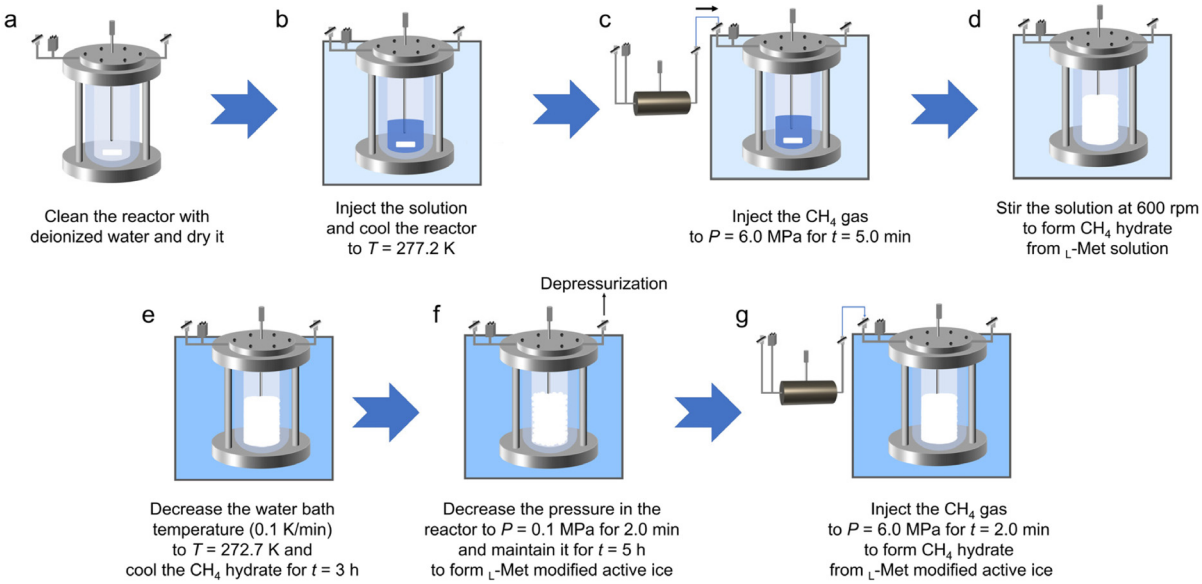

Fig. 2 Schematic diagram of the experimental procedure for (a)–(f) synthesizing L-Met modified active ice, and (g) subsequent CH_4 hydrate formation.

a thermostatic water bath for precooling. A CH_4 gas storage tank (precooled to 271.2 K) was used to inject CH_4 into the reactor at an initial pressure of 0.3 MPa to remove residual gas three times. Upon stabilization of the reactor temperature at 277.2 K, CH_4 gas was introduced until the pressure reached 6.0 MPa. Then, magnetic stirring was initiated at 600 rpm and kept stable for 3 h. Next, the water bath temperature was reduced to 272.7 K at a controlled rate of 0.1 K min^{-1} and held constant for an additional 3 h to ensure complete CH_4 hydrate formation and stabilization.

(II) CH_4 hydrate dissociation to form L-Met modified active ice: following CH_4 hydrate formation and temperature stabilization at 272.7 K, the stirring was terminated and the reactor was depressurized at a constant rate of 0.01 MPa s^{-1} (see Fig. 2f). Upon reaching 0.1 MPa, the outlet valve remained open for 5 h to ensure complete CH_4 hydrate dissociation. The solid residue remaining in the reactor was the L-Met modified active ice.

(III) CH_4 hydrate formation from L-Met modified active ice: after 5 h of stabilization, the reactor was repressurized with CH_4 gas at a controlled rate of 0.1 MPa s^{-1} using the precooled CH_4 storage tank (maintained at 272.7 K) until the pressure reached 6.0 MPa in the reactor, thereby inducing rapid CH_4 hydrate reformation (see Fig. 2g). The experiment was concluded once the pressure drop in the reactor had stabilized to below 0.01 MPa h^{-1}.

2.4. Calculation method

This study presents distinct methodological approaches for quantifying CH_4 uptake in L-Met solution and L-Met modified active ice systems. In conventional L-Met solution systems, CH_4 uptake is calculated using standard procedures as described in our previous work considering CH_4 dissolution.[29] In contrast, the active ice system demonstrates immediate nucleation characteristics during the CH_4 gas injection process, necessitating the development of a dynamic computational model based on molar balance principles.[27] The baseline time t = 0 was defined as the moment of CH_4 hydrate nucleation, identified by a deflection point on the P–T trajectory in relation to CH_4 hydrate phase equilibria (see Fig. S16). At time t, the molar balance can be expressed as:

$$n_{\mathrm{in},t} = n_{\mathrm{gas},t} + n_{\mathrm{hydrate},t} \quad (1)$$

where $n_{\mathrm{hydrate},t}$ represents the molar quantity of CH_4 gas consumed in CH_4 hydrate formation at time t, which is calculated as follows:

$$n_{\mathrm{hydrate},t} = \frac{m_{\mathrm{w}} C_{\mathrm{w}}}{M_{\mathrm{w}} N_{\mathrm{h}}} \quad (2)$$

where m_{w} and M_{w} represent the initial mass of water (ice) in g and the molar mass of water in g mol^{-1}. C_{w} is the ratio of water converted to CH_4 hydrate. N_{h} represents the hydration number, taken as 6.0 in this work.[27]

$n_{\mathrm{in},t}$ is the molar quantity of gas injected into the reactor, which is calculated as follows:

$$n_{\mathrm{in},t} = \frac{P_{\mathrm{s},0} V_{\mathrm{s,gas}}}{Z_{\mathrm{s},0} R T_{\mathrm{s},0}} - \frac{P_{\mathrm{s},t} V_{\mathrm{s,gas}}}{Z_{\mathrm{s},t} R T_{\mathrm{s},t}} \quad (3)$$

where P_{s}, T_{s}, and Z_{s} represent the pressure in Pa, the temperature in K, and the compressibility factor in the gas storage tank, respectively. 0 and t represent the initial time and time t during each experimental run; the unit is min. The compressibility factor (Z) was calculated using the Peng–Robinson EOS accounting for the non-ideal gas behaviour at high pressure.[30] $V_{\mathrm{s,gas}}$ represents the volume of the gas storage tank, and the unit is m^3. R is the universal gas constant, taken as 8.314 J

$(\text{mol K})^{-1}$. $n_{\text{gas},t}$ represents the molar quantity of the remaining CH_4 gas in the reactor at time t, which is calculated as follows:

$$n_{\text{gas},t} = \frac{P_{\text{r},t} V_{\text{r,gas}}}{Z_{\text{r},t} R T_{\text{r},t}} \quad (4)$$

where $P_{\text{r},t}$, $T_{\text{r},t}$, and $Z_{\text{r},t}$ represent the pressure, the temperature, and the compressibility factor in the reactor at time t, respectively. $V_{\text{r,gas}}$ represents the volume of the gas phase of the reactor, and the unit is m^3. It is calculated as follows:

$$V_{\text{r,gas}} = V_{\text{r}} - V_{\text{stirrer}} - 1.25 V_{\text{w}} C_{\text{w}} - 1.087 V_{\text{w}} (1 - C_{\text{w}}) \quad (5)$$

where V_{r}, V_{stirrer}, and V_{w} represent the volumes of the reactor, stirrer and initial water in m^3, respectively. 1.25 and 1.09 are the volume expansion factors of CH_4 hydrate and active ice with reference to water. C_{w} represents the conversion rate of active ice to CH_4 hydrate after the experiment.[27] Then, the CH_4 gas uptake (n_{g}) in $V_{\text{g}}/V_{\text{w}}$ is calculated as follows:

$$n_{\text{g}} = \frac{0.0224 n_{\text{hyarate},t}}{V_{\text{w}}} \quad (6)$$

The growth rate is characterized by t_{90} (time required to achieve 90% final CH_4 uptake). All experiments were independently repeated at least twice to ensure data reliability and reproducibility.

3. Results and discussion

3.1. Kinetics of L-Met modified active ice synthesis and ultra-rapid CH_4 hydrate formation

The L-Met modified active ice was synthesized based on previously established procedures.[27] It is worth mentioning that L-Met, a green and environmentally friendly amino acid, was employed as the kinetic hydrate promoter instead of sodium dodecyl sulfate (SDS).[31] Fig. 3 illustrates the morphological evolution of active ice synthesis and its application in promoting CH_4 hydrate formation. The process was divided into three distinct stages. During stage I, CH_4 hydrate formation primarily occurred at the 1st formation stage, with the CH_4 uptake reaching 114.21 $V_{\text{g}}/V_{\text{w}}$ (see Fig. 3a). Morphological observations showed that the CH_4 hydrate nucleated in the bulk solution, gradually forming a slurry-like CH_4 hydrate that extended toward the gas phase and adhered to the reactor walls (see Fig. 3b and Video SV1). Upon cooling to 272.7 K, the total CH_4 uptake increased to 151.39 $V_{\text{g}}/V_{\text{w}}$ until the end of the 2nd formation stage. The L-Met induced loose and porous structure facilitated capillary-driven transport to the gas–hydrate interface. This transport resulted in alternating bright and dark patterns on the CH_4 hydrate surface during the process. The detailed promotion mechanism of amino acid solution on CH_4 hydrate formation has been reported in our previous work.[32] However, overall CH_4 hydrate growth remained relatively slow (t_{90} = 242.81 min), primarily due to intrinsic limitations in heat and mass transfers within the system.

In stage II, the rapid pressure drop caused a sharp decrease in temperature, which then gradually increased as the pressure reached atmospheric level (see Fig. 3c). Depressurization below the phase equilibrium (2.52 MPa at 272.7 K for CH_4 hydrate)[33] triggered CH_4 hydrate dissociation on the surface. Subsequently, it was observed that the dissociated water did not liquefy but refroze rapidly, generating the "L-Met modified active ice". This newly formed active ice preserved the original CH_4 hydrate morphology and porous structure (see Fig. 3d and Video SV2). The CH_4 hydrate formation in the next stage began only after both temperature and pressure were fully stabilized. This ensured that the CH_4 gas had been completely released from the dissociated hydrate.

During stage III, CH_4 hydrate nucleated at the active ice surface once the pressure reached about 3.1 MPa. This nucleation occurred immediately after the pressure slightly surpassed the phase equilibrium by approximately 0.6 MPa, demonstrating the activity of active ice in promoting nucleation. The variations in temperature and pressure, along with the corresponding phase equilibrium curves, are shown in Fig. S16. In conventional L-Met solution systems, CH_4 hydrate formation typically requires a finite induction time even after reaching the target pressure. Another key observation is that the formation proceeds at an ultra-rapid rate (t_{90} = 2.84 min) while maintaining a high CH_4 uptake of 158.96 $V_{\text{g}}/V_{\text{w}}$ (see Fig. 3e). The accuracy of the CH_4 uptake calculation based on the mole balance and volume balance method was independently validated by performing complete CH_4 hydrate dissociation experiments (see Fig. S18). Previous studies revealed that the active ice developed a porous structure with interconnected channels. This unique architecture allowed CH_4 molecules to adsorb onto newly formed gas–liquid–solid interfaces, thereby accelerating CH_4 hydrate formation.[27,34]

Morphological observations indicated that CH_4 hydrate initially nucleated on the ice surface. It then grew inward into the ice interior, with ice melting and CH_4 hydrate formation occurring simultaneously. At the end of the growth process, CH_4 hydrate growth remained confined within the ice layer without significant outward expansion (see Fig. 3f and Video SV3). Importantly, L-Met modified active ice accelerates CH_4 hydrate formation without compromising overall gas storage capacity. Moreover, the use of environmentally benign L-Met underscores its potential for sustainable and efficient SNG technologies.

3.2. Micro-kinetics of ultra-rapid CH_4 hydrate formation from L-Met modified active ice using *in situ* Raman spectroscopy

To elucidate the molecular-level mechanisms underlying L-Met modified active ice synthesis and its role in promoting subsequent CH_4 hydrate formation, *in situ* Raman spectroscopy was carried out throughout the three stages.[35] The different states of CH_4 molecules including gaseous CH_4, dissolved CH_4, and CH_4 hydrate were first measured independently (see Fig. S2). This enabled an analysis of how CH_4 was distributed among the phases. Importantly, this study simultaneously monitors CH_4 cage occupancy and the evolution of water vibrational modes. Gaussian fitting of the Raman spectra

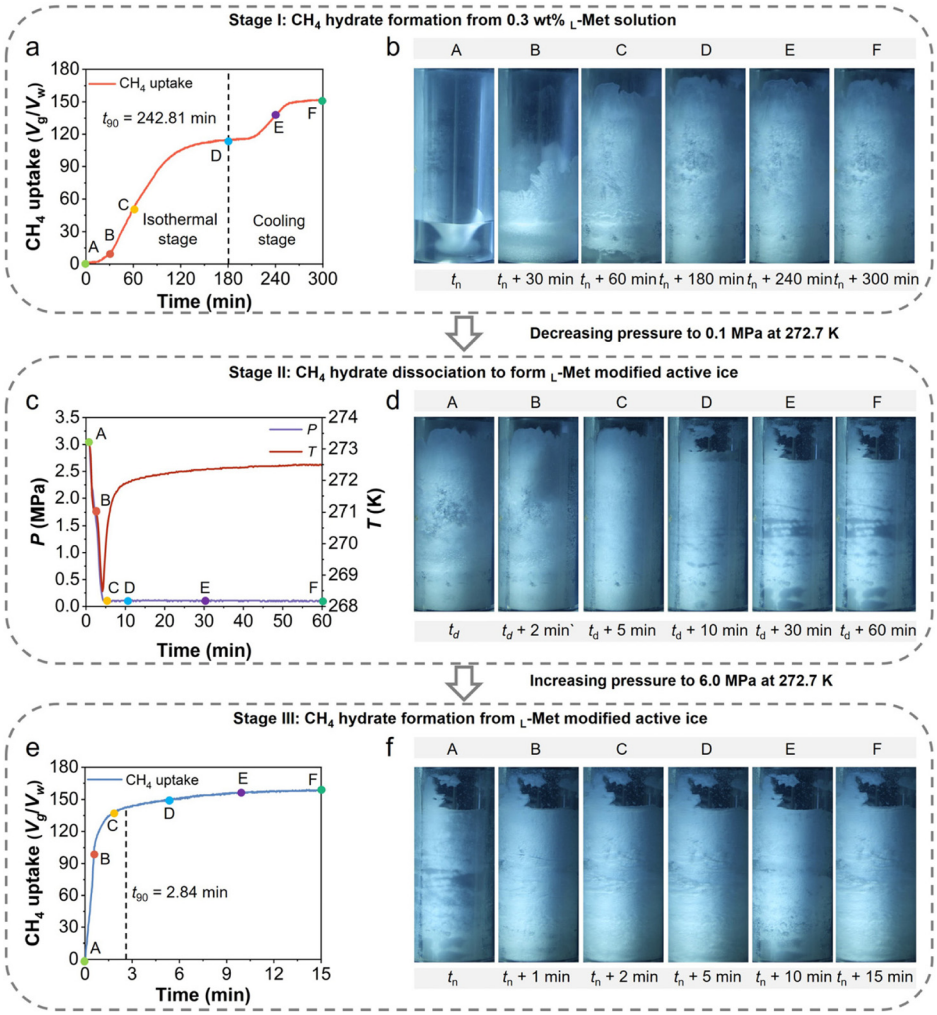

Fig. 3 (a) CH_4 uptake profile and (b) CH_4 hydrate morphology evolution in stage I: CH_4 hydrate formation from 0.3 wt% L-Met solution at initial P = 6.0 MPa and T = 277.2 K (1st formation stage) and subsequent T = 272.7 K (2nd formation stage). (c) P–T and (d) morphology evolution for stage II: CH_4 hydrate dissociation to form L-Met modified active ice (P = 0.1 MPa, T = 272.7 K). (e) CH_4 uptake profile and (f) CH_4 hydrate morphology evolution for stage III: CH_4 hydrate formation from the L-Met modified active ice (P = 6.0 MPa, T = 272.7 K).

enables quantitative tracking of real-time changes in the hydrogen bond network.[36,37] This method provides a detailed description of the structural transition from active ice to CH_4 hydrate and offers mechanistic insights into the ultra-rapid formation process.

Fig. 4a and b show the time-dependent *in situ* Raman spectroscopy during CH_4 hydrate formation from 0.3 wt% L-Met solution, with the corresponding temperature–pressure profiles shown in Fig. S3. Dissolved CH_4, identified by the Raman peak at 2910.1 cm^{-1}, was first detected at 60 min, accompanied by a gradual increase in water peak intensity. Minimal changes were observed until 180 min. As the temperature decreased to 272.7 K, CH_4 hydrate nucleation commenced around 300 min. This was indicated by the appearance of peaks at 2905.2 and 2917.2 cm^{-1}, which correspond to CH_4 molecules occupying the $5^{12}6^2$ large and 5^{12} small cages, respectively.[38] The intensity ratio (3 : 1) closely matched the theoretical occupancy ratio of CH_4 hydrate.

Between 360 and 420 min, the measured Raman peak intensities at 2905.2 and 2917.2 cm^{-1} deviated from the theoretical values. Additionally, new peaks emerged near the water region at 3019.6 and 3069.1 cm^{-1}, which correspond to the C–H asymmetric stretch (ν_3) of gaseous CH_4 and the C–H overtone of the asymmetric bend ($2\nu_2$), respectively.[36] Detailed evidence and analysis are shown in Fig. S4 and the SI. Simultaneously, the persistence of the 2905.2 cm^{-1} shoulder Raman peak confirmed the presence of CH_4 hydrate. Meanwhile, the Raman peak at 2917.2 cm^{-1} indicated the coexistence of CH_4 molecules in 5^{12} small cages and the gas phase. These features suggest that the formed CH_4 hydrate may possess a relatively porous structure, containing both encapsulated and free CH_4 molecules.

To further investigate the evolution of the hydrogen bond network of water molecules, we performed Gaussian fitting of the O–H stretching band (2800–3700 cm^{-1}). The analysis was applied to CH_4 hydrate formed in L-Met solution, L-Met modi-

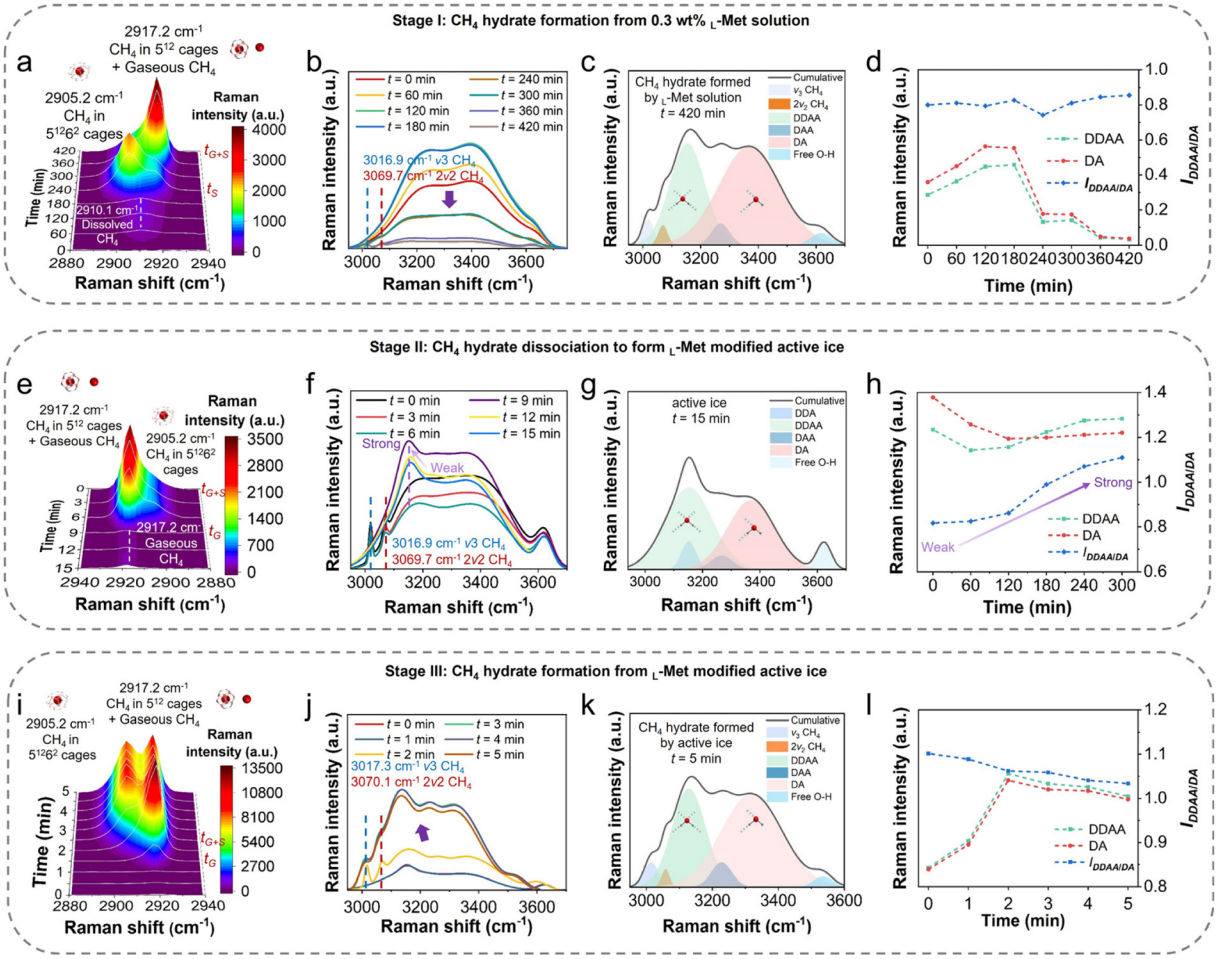

Fig. 4 Time-dependent *in situ* Raman spectroscopy during different stages of CH_4 hydrate formation and dissociation: CH_4 hydrate formation from 0.3 wt% L-Met solution (stage I) showing (a) CH_4 Raman peak evolution over 2880–2940 cm^{-1}, (b) water Raman peak evolution over 2940–3700 cm^{-1}, (c) Gaussian fitting of O–H stretching peaks in CH_4 hydrate formed by 0.3 wt% L-Met solution, and (d) water network vibrational intensity evolution of double donor–double acceptor hydrogen bonds (DDAA), single donor–single acceptor hydrogen bonds (DA) and their ratio ($I_{DDAA/DA}$). CH_4 hydrate dissociation to form active ice (stage II) showing (e) CH_4 Raman peak evolution, (f) water Raman peak evolution, (g) Gaussian fitting of O–H stretching peaks in active ice, and (h) evolution of DDAA, DA and $I_{DDAA/DA}$. CH_4 hydrate formation from the active ice (stage III): (i) CH_4 Raman peak evolution, (j) water Raman peak evolution, (k) Gaussian fitting of O–H stretching peaks in CH_4 hydrate formed by active ice, and (l) evolution of DDAA, DA, and $I_{DDAA/DA}$.

fied active ice, and CH_4 hydrate formed from the active ice. Moreover, the Gaussian fitting results for the L-Met solution are also provided in Fig. S12. The ratio of double donor–double acceptor (DDAA) to single donor–single acceptor (DA) hydrogen bonds ($I_{DDAA/DA}$) served as a metric for hydrogen bond ordering. During stage I, $I_{DDAA/DA}$ exhibited only a minor increase from 0.80 to 0.83 (Fig. 2d), indicating that the hydrogen bond network of the formed CH_4 hydrate remains largely comparable to that of the initial L-Met solution.

In situ Raman spectroscopy was also acquired during the dissociation of CH_4 hydrate into L-Met modified active ice. This was done to monitor changes in both the CH_4 molecules and the hydrogen bond network of water molecules (see Fig. 4e and f).

The corresponding temperature and pressure results are shown in Fig. S5. The Raman peak at 2917.2 cm^{-1}, which represents CH_4 in 5^{12} small cages and the gas phase, rapidly decreased within 9 min of depressurization. This occurred alongside the disappearance of the ν_3 and $2\nu_2$ CH_4 bands. The Raman peak at 2917.2 cm^{-1} persisted throughout the experiment. Its relatively weak intensity indicates the presence of only a small amount of gaseous CH_4. This interpretation is supported by our previous confirmation that gaseous CH_4 is detectable even at 0.1 MPa (see Fig. S4). Interestingly, the water Raman peak at lower shifts (3100–3300 cm^{-1}) gradually intensified during the formation of active ice (see Fig. 4f). In the first 60 min, both DDAA and DA decreased, indicating the onset of CH_4 hydrate dissociation, while their ratio slightly increased. Between 60 and 240 min, DA continued to decrease, and DDAA increased, resulting in an increase of the ratio from 0.83 to 1.10 (see Fig. 4h). Thereafter, no significant changes were observed, suggesting that the hydrogen bond network in

active ice became well-organized. It is worth noting that all subsequent kinetic experiments were conducted after at least 300 min to ensure that the hydrogen bond network of active ice was fully established.

Fig. 4i and j illustrate the evolution of CH_4 vibrational features and water O–H stretching bands during CH_4 hydrate formation from 0.3 wt% L-Met modified active ice. The corresponding temperature–pressure evolution is shown in Fig. S6. Within 2 min, a Raman peak at 2917.2 cm^{-1} appeared, while the characteristic hydrate peak at 2905.2 cm^{-1} was absent. The concurrent emergence of the $2\nu_2$ and ν_3 CH_4 modes at 3017.3 and 3070.1 cm^{-1} indicated that the 2917.2 cm^{-1} peak at this stage originated from gaseous CH_4. At 2.5 min, the characteristic Raman peak of CH_4 hydrate at 2905.2 cm^{-1} became evident, coexisting with Raman peak of gaseous CH_4. Gaussian fitting of the CH_4 Raman peaks was then performed to determine the relative contributions of gaseous CH_4 and CH_4 hydrate (see Fig. S11). We also calculated both the cage occupancies and hydration numbers by analysing the deconvoluted Raman spectra and adopting the van der Waals–Platteeuw (vdW–P) statistical thermodynamic model.[39] For the solution system, the average occupancies of small and large cages are 87.86% and 98.12%, respectively, whereas in the L-Met active ice system, the corresponding values increase to 92.05% and 97.78%. These results indicate that the active ice system enhances the small cage occupancy (see Fig. S13). Moreover, the observed cage occupancy is similar to those reported for the L-tryptophan modified active ice system.[28] The average hydration numbers for CH_4 hydrate formed from L-Met solution and L-Met active ice are 6.10 and 6.04, respectively. Although the hydration numbers derived from Raman spectra deviate slightly from the theoretical values, sensitivity analysis indicates that this deviation has a negligible impact on the calculated CH_4 uptake (Fig. S14).

The *in situ* Raman study first detected gaseous CH_4, followed by the coexistence of CH_4 hydrate and gaseous CH_4 peaks. Based on this sequence, we speculated on the possible probe positions relative to the L-Met modified active ice and CH_4 hydrate during this process (see Fig. S15). As CH_4 hydrate began to form, the probe was gradually encapsulated by the CH_4 hydrate crystals. Subsequently, the formation of active ice nearly preserved the original morphology of CH_4 hydrate, so the Raman probe remained almost entirely enclosed within the active ice.

Upon reinjection of CH_4 gas, the increased gas temperature caused rapid melting of the active ice surface, and CH_4 quickly nucleated on the active ice surface to form CH_4 hydrate. However, the ice near the probe only partially melted and had not yet transformed into CH_4 hydrate. Therefore, the Raman signal first detected a distinct gaseous CH_4 Raman peak. As the melting region expanded, more CH_4 gas accumulated near the probe, and the gas-phase peak intensity gradually increased.

After approximately 2.5 min, the L-Met modified active ice within the laser spot region transformed into CH_4 hydrate. This transformation was marked by the appearance of a characteristic peak at 2905.2 cm^{-1}, which corresponds to CH_4 molecules occupying the $5^{12}6^2$ large cages of CH_4 hydrate. Subsequently, as the laser spot likely illuminated both the porous hydrate and adjacent gas regions, the Raman spectra still exhibited the coexistence of gaseous CH_4 and CH_4 hydrate. No Raman signals of dissolved CH_4 were observed during stage III, suggesting that CH_4 dissolution did not occur at this stage. The evolution of water hydrogen bond ordering is shown in Fig. 4l, decreasing slightly from 1.10 to 1.03, which suggests that CH_4 hydrate formation from active ice modestly perturbed the local hydrogen bond network.

3.3. Optimizing L-Met concentration for effective active ice synthesis and superior CH_4 hydrate kinetics

The influence of L-Met concentration on CH_4 hydrate formation was systematically examined in both solution and L-Met modified active ice systems to elucidate its tuning effect on CH_4 hydrate formation kinetics and morphology. In the L-Met solution system, CH_4 hydrate formation proceeded slowly despite increasing L-Met concentration (see Fig. 5a and b). This suggests that the process remained constrained by heat and mass transfer limitations in the bulk solution. At the optimal 0.3 wt% L-Met, CH_4 uptake reached 154.48 ± 3.63 V_g/V_w with a t_{90} of 242.84 ± 0.47 min, representing only a modest improvement over pure water (see Table S5).

In contrast, the active ice system exhibited ultra-rapid CH_4 hydrate formation and strong sensitivity to L-Met concentration (see Fig. 5c and d). In the absence of L-Met, CH_4 uptake was limited to 12.29 ± 0.57 V_g/V_w, and 0.03 wt% L-Met induced only partial acceleration (t_{90} = 10.54 ± 1.53 min). Strikingly, 0.3 wt% L-Met yielded the fastest kinetics, reaching a t_{90} of only 3.33 ± 0.43 min, the highest uptake (156.05 ± 3.28 V_g/V_w), and a water conversion of 72.24%. At a higher concentration of 3.0 wt%, both CH_4 uptake and growth rate declined. This demonstrates that CH_4 hydrate formation in the active ice system is highly tunable through L-Met concentration, with the optimal level for maximal growth kinetics being around 0.3 wt%. Based on the real-time temperature and pressure measurements, the L-Met modified active ice system shows no significant temperature increase during rapid CH_4 hydrate formation, whereas the L-Met solution exhibits multiple pronounced temperature increases (see Fig. S20). One plausible reason is that the heat released from CH_4 hydrate formation (55.44 kJ mol^{-1} CH_4 hydrate) can be partially neutralized by the melting of active ice (35.94 kJ for N_h mol of H_2O), which creates a sustained feedback loop for CH_4 hydrate growth.[27]

The kinetic results are comparable to those reported for the L-tryptophan modified active ice system (t_{90} = 2.42 ± 0.64 min, CH_4 uptake = 146.56 ± 5.72 V_g/V_w),[28] confirming the excellent promotion performance of the L-Met modified active ice. Additionally, we further validated the ultra-rapid CH_4 hydrate kinetics across scales in a series of reactors of different volumes (*i.e.*, 125.0 mL, 256.4 mL and 626.8 mL). The kinetic results suggest that ultra-rapid CH_4 hydrate formation was achieved across scales with an average t_{90} of 3.3 min and a final average gas uptake of 156.9 V_g/V_w. Thus, the conventional

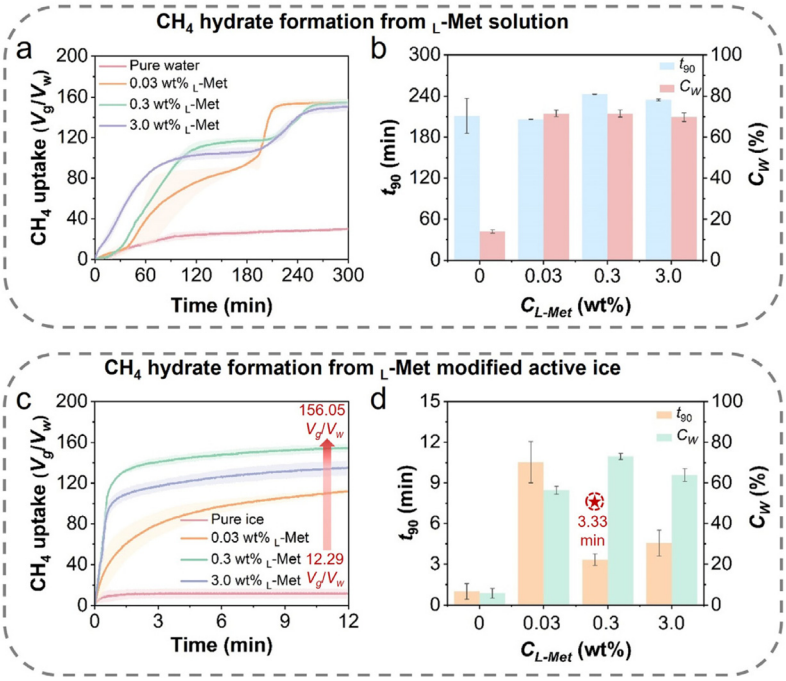

Fig. 5 (a) CH_4 uptake profiles and (b) t_{90} (time required to achieve 90% final CH_4 uptake), and C_w (final conversion rate of water to CH_4 hydrate) during CH_4 hydrate formation with different concentrations of L-Met (0–3.0 wt%) at initial P = 6.0 MPa, T = 277.2 K (1st stage) and T = 272.7 K (2nd stage). (c) CH_4 uptake profiles and (d) t_{90} and C_w during CH_4 hydrate formation at P = 6.0 MPa and T = 272.7 K.

mass transfer resistance due to CH_4 diffusion across the gas–liquid interface was not observed and is not the limiting factor for the proposed active ice method (see Fig. S21).

Morphological evolution across the three stages further reveals that an intermediate L-Met concentration optimally balances the active ice microstructure and defect density. This balance critically governs CH_4 hydrate nucleation, growth, and the observed ultrarapid CH_4 uptake (see Fig. S23–S25). In the L-Met solution system, CH_4 hydrate forms sparse, stratified films at a low concentration (0.03 wt%) and dense, block-like aggregates at a high concentration (3.0 wt%). These distinct morphologies reflect limited control over nucleation and gas–liquid contact in the solution system. In contrast, the active ice system exhibited a pronounced dependence on amino acid concentration. At the optimal 0.3 wt% L-Met, the active ice maintained continuous surface coverage and structural integrity, maximizing gas–liquid contact and enabling ultra-rapid nucleation and inward propagation of CH_4 hydrate growth.

3.4. Microscopic morphology and hydrogen bond network characterization in L-Met modified active ice

To gain a deeper understanding of the modifying effect of L-Met on the microscopic morphology of active ice, we conducted cryogenic scanning electron microscopy (Cryo-SEM). The results show that pure ice exhibits a smooth, dense surface with negligible porosity. This compact structure severely restricts the gas–ice contact, limiting CH_4 hydrate formation. Interestingly, the 0.3 wt% L-Met modified active ice exhibits an overall well-connected porous structure, with its surface showing open and larger pores ranging from 7 to 17 μm, as shown in Fig. 6b. This topology significantly enhances the CH_4 diffusion. However, at the higher concentration of 3.0 wt% (see Fig. 6c), the ice structure became notably more compact; the pores transformed into closed and smaller structures (about 4 μm). Quantitative analysis of the SEM images indicates that the pore area fractions of the 0.3 wt% and 3.0 wt% L-Met modified active ice are 22.1% and 16.1%, respectively (see Fig. S32).

The spatial distribution of L-Met molecules on the surface of modified active ice was further examined using surface elemental mapping based on cryogenic scanning electron microscopy (Cryo-SEM) and energy-dispersive X-ray spectroscopy (EDS). The results show that the oxygen (O) signal represents the distribution of water molecules forming the ice lattice, while the nitrogen (N) and sulfur (S) signals serve as elemental markers for L-Met molecules. The O maps in pure ice confirm the uniform distribution of water molecules forming the ice lattice (see Fig. 6d). The 0.3 wt% L-Met modified active ice exhibits larger and more open pores, whereas the 3.0 wt% L-Met modified active ice shows closed and smaller pores (see Fig. 6e and f). Meanwhile, the N and S distributions indicate that L-Met molecules are homogeneously distributed on the ice surface at both concentrations.

To gain molecular-level insight into the modification of active ice by L-Met, the effect of L-Met concentration on the hydrogen bond network was examined using *in situ* Raman spectroscopy by analyzing the O–H stretching region (2800–3700 cm^{-1}), as shown in Fig. 6g and h. It is worth

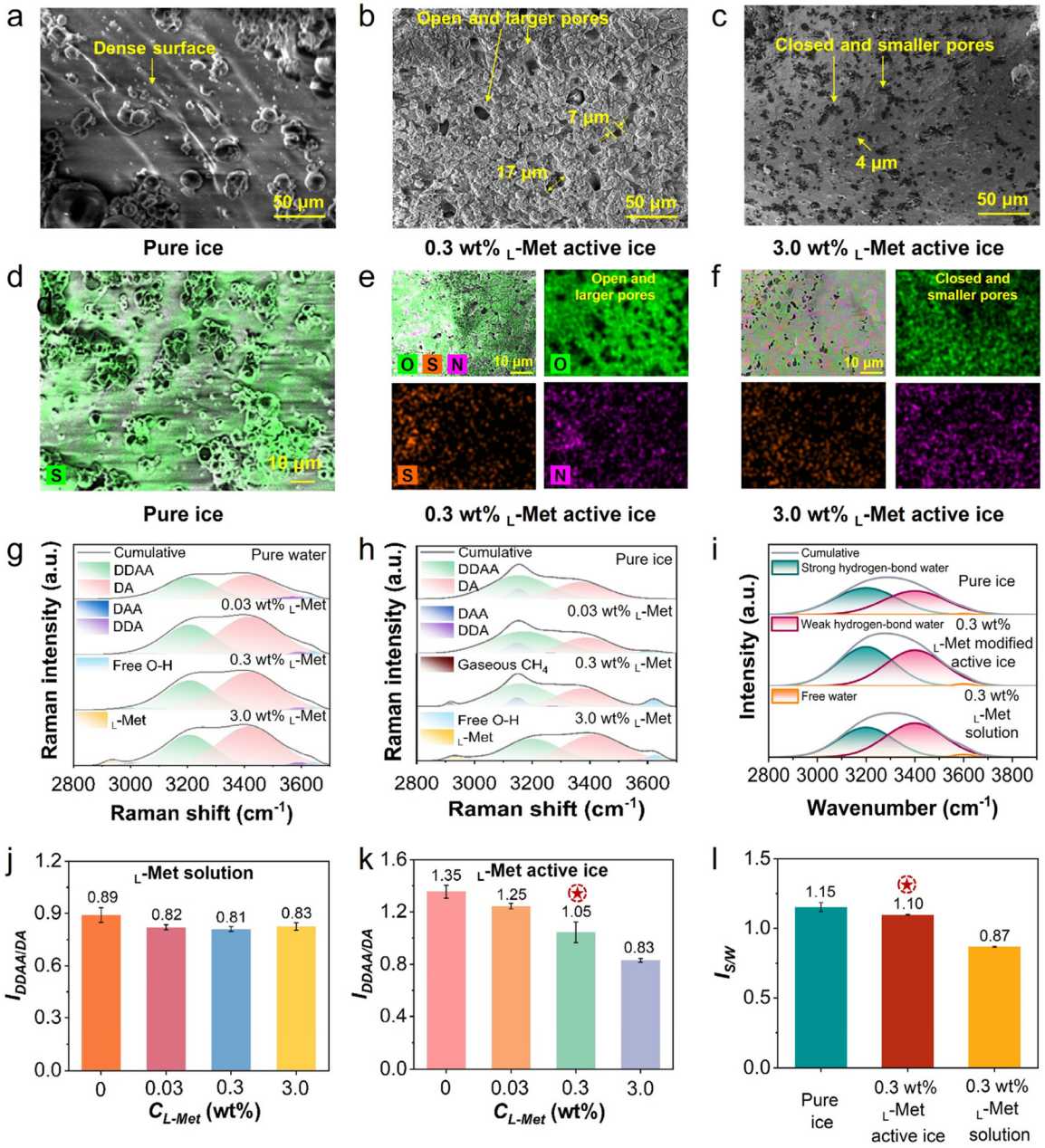

Fig. 6 Cryogenic scanning electron microscopy (Cryo-SEM) image for (a) pure ice, (b) 0.3 wt% L-Met modified active ice, and (c) 3.0 wt% L-Met modified active ice. Energy dispersive spectroscopy (EDS) elemental mapping for (d) pure ice, (e) 0.3 wt% L-Met modified active ice, and (f) 3.0 wt% L-Met modified active ice. Acquired Raman spectroscopy and corresponding Gaussian fitting of water O–H stretching region (2800–3700 cm^{-1}) for different concentrations of (g) L-Met solution and (h) L-Met modified active ice. (i) Acquired Fourier transform infrared (FT-IR) spectroscopy and corresponding Gaussian fitting of water O–H stretching region (2800–3900 cm^{-1}) for pure ice, 0.3 wt% L-Met modified active ice, and 0.3 wt% L-Met solution. Comparison of the $I_{DDAA/DA}$ ratios derived from the fitted results for different concentrations of (j) L-Met solution and (k) L-Met modified active ice. (l) Comparison of the intensity ratio of the strong hydrogen bond peak to the weak hydrogen bond peak ($I_{S/W}$) derived from the fitted results for pure ice, 0.3 wt% L-Met modified active ice, and 0.3 wt% L-Met solution.

emphasizing that the spectral deconvolution strategy employed in this study, relying on rigorous baseline subtraction and multi-peak Gaussian fitting, aligns with standard analytical protocols widely reported in the literature.[36] Detailed fitting methodology and sensitivity analysis are included in the SI. Compared with pure water, all L-Met solutions exhibited a slight reduction in the DDAA component and a relative increase in the DA fractions, indicating a mild disordering of the hydrogen bond network. At a higher concentration (3.0 wt%), an additional Raman feature at 2931.1 cm^{-1} emerged, attributed to the C–H stretching of L-Met.[37]

However, the hydrogen bond network in the L-Met modified active ice system exhibits a distinctly different behaviour. As shown in Fig. 6h, pure ice possesses a highly ordered hydrogen

bond network, as reflected by a strong and well-defined O–H stretching band dominated by tetrahedral hydrogen-bond configurations. Interestingly, the O–H stretching band progressively weakened and broadened with increasing L-Met concentrations, reflecting gradual disruption of the ordered hydrogen bond network in active ice. At higher concentrations, a weak gaseous CH_4 band appeared at 0.3 wt%. Additionally, the characteristic C–H stretching of L-Met was detected in both the solution and active ice systems at 3.0 wt%. To further enhance the reliability of our interpretation regarding the structural evolution of the hydrogen bond network, Fourier transform infrared (FT-IR) spectroscopy analysis was conducted. As shown in Fig. 6i, the O–H stretching vibration bands of the L-Met modified active ice and pure ice exhibit a distinct red-shift towards lower wavenumbers compared to the L-Met solution, indicating a strengthening of hydrogen bond interactions upon freezing.

Quantitative analysis reveals that the effect of L-Met on the hydrogen-bond network differs markedly between the solution and active ice systems. In the L-Met solution, the overall $I_{DDAA/DA}$ ratio remains between 0.80 and 0.89 (Fig. 5j), indicating that L-Met induces only a slight disruption of the water hydrogen bond network. In contrast, the L-Met modified active ice system exhibits a much higher degree of hydrogen bond ordering, with $I_{DDAA/DA}$ decreasing systematically from 1.35 ± 0.05 for pure ice to 1.25 ± 0.02, 1.05 ± 0.08, and 0.83 ± 0.01 as the L-Met concentration increases from 0.03 to 3.0 wt% (Fig. 5h and Table S4), reflecting progressive disruption of the ordered hydrogen bond network in the solid state. Notably, at the optimal 0.3 wt% L-Met modified active ice maintains a partially ordered hydrogen bond network, which correlates with its superior CH_4 hydrate formation kinetics. Complementary FT-IR measurements also confirm these observations. The intensity ratio of strong to weak hydrogen bonds ($I_{S/W}$, Fig. 6l) shows that pure ice exhibits the highest hydrogen bond ordering (1.15 ± 0.03) and the 0.3 wt% L-Met solution displays a more disordered hydrogen bonding network (0.87 ± 0.01). Notably, the 0.3 wt% L-Met modified active ice exhibits an intermediate value (1.10 ± 0.01), reflecting a partially ordered hydrogen bond network, as also evidenced in the Raman spectra analysis (see Fig. 6l).

The multi-scale characterization results suggest that the superior kinetic performance of the 0.3 wt% L-Met modified active ice system stems from a synergistic interplay between physical and chemical factors. Specifically, the loose and porous structure of modified active ice, together with the uniform distribution of L-Met, ensures efficient gas–solid contact and CH_4 diffusion. We further designed experiments to identify the key process factor that yields the superior kinetic performance. Hydrophilic amino acid L-arginine modified active ice does not exhibit a promotion effect, with final CH_4 uptake achieved only 13% of that for L-Met active ice (see Fig. S26). Additionally, the CH_4 hydrate formation rate is relatively slow in the L-Met solution system compared with that in the active ice system, as evidenced by the significantly longer t_{90} of 26.3 min (see Fig. S27). It is also verified that the active ice method is sensitive to temperature, since a temperature increment of only 0.5 K close to the ice melting point yielded a 23.7% lower final CH_4 uptake (see Fig. S28). At higher L-Met concentrations, this synergy is disrupted, leading to a collapse of the porous structure and excessive disruption of the hydrogen bond network, resulting in inferior CH_4 hydrate formation kinetics. Based on the above experimental evidence, the partially ordered hydrogen bond network modified by the optimal L-Met concentration provides a favourable environment for fast CH_4 diffusion and enclathration, which is also corroborated by the spectral analysis discussed above.

3.5. Proposed mechanism of ultra-rapid CH_4 hydrate formation kinetics from L-Met modified active ice

Fig. 7 illustrates the proposed promotion mechanism for CH_4 hydrate formation from L-Met modified active ice. For pure ice, the rigid and highly ordered hydrogen bond network (see Fig. 7a) restricts the rearrangement of water molecules required for CH_4 hydrate formation. Upon the introduction of L-Met, which is uniformly distributed across the ice surface, the hydrogen bond network of ice is modified. Specifically, the amine group of L-Met acts as a hydrogen bond donor to water oxygen atoms, whereas the carboxyl group serves as a hydrogen bond acceptor from water hydrogen atoms, thereby forming additional hydrogen bonds independently with water molecules.[37] These interactions thus reduce the overall hydrogen bond ordering. At an optimal concentration (0.3 wt%), L-Met modified active ice exhibits a partially ordered hydrogen bond network, which is favourable for the rapid rearrangement of water molecules into CH_4 hydrate cages (see Fig. 7b).[28] However, at a lower concentration (0.03 wt%), L-Met fails to sufficiently modify the rigid hydrogen bond network of ice. In contrast, a higher concentration (3.0 wt%) causes excessive modification, leading to a disordered hydrogen bond network. This structural degradation results in hydrogen bond ordering as low as that in the L-Met solution system, ultimately hindering the incorporation of CH_4 molecules (see Fig. 7c).

An additional advantage of the active ice method in promoting CH_4 hydrate kinetics is the plausible energy feedback loop, which involves sustained CH_4 hydrate formation fuelling active ice melting (see Fig. 7d).[27] Specifically, heat released during CH_4 hydrate formation is absorbed by adjacent active ice, causing the ice layer to melt. The melt-water, in turn, serves as the source for forming new CH_4 hydrate. This dynamic cycle drives the outward-to-inward progression of CH_4 hydrate formation, progressively converting the active ice into loose and porous CH_4 hydrate within minutes (see Fig. 7e). The mitigation of fast heat release due to rapid CH_4 hydrate formation is fundamentally resolved in the active ice method and is significantly different from that in the conventional gas–liquid system. Furthermore, based on Raman spectra and cage occupancy analysis, CH_4 hydrate formed from active ice exhibits a high occupancy of 5^{12} small cages compared with that formed from L-Met solution, reflecting the favourable encapsulation of guest molecules under these conditions (see Fig. 7f). Overall, L-Met modified active ice enables

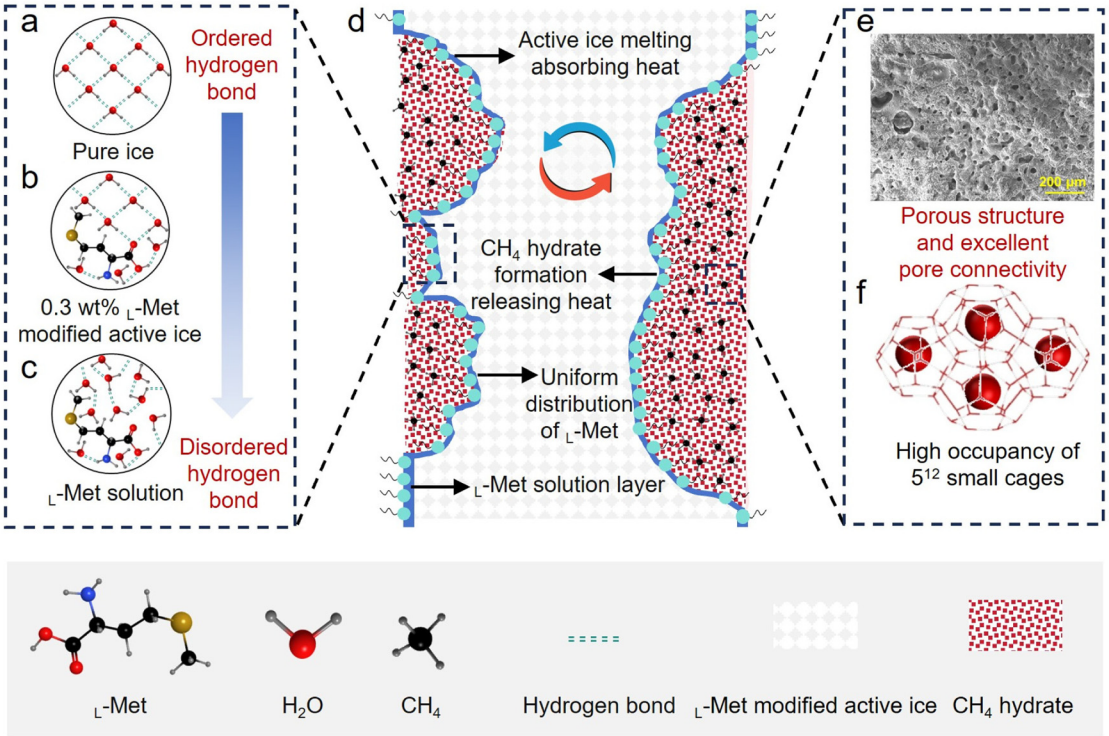

Fig. 7 Schematic showing the proposed mechanism of CH_4 hydrate formation from L-Met modified active ice: hydrogen bond network of (a) pure ice, (b) 0.3 wt% L-Met modified active ice, and (c) L-Met solution, showing the decreasing hydrogen bond ordering with increasing L-Met concentrations. (d) Simultaneous active ice melting and CH_4 hydrate formation; CH_4 hydrate formed from active ice exhibits (e) a porous structure and (f) high occupancy of 5^{12} small cages of CH_4 hydrate.

rapid CH_4 hydrate formation and high CH_4 storage capacity. This is achieved by modifying the hydrogen bond network and microstructure of active ice. This approach provides an effective strategy for designing green and sustainable SNG technology.

We further evaluated the chemical cost of L-Met used as the promoter to modify active ice for CH_4 hydrate storage by using the optimal 0.3 wt% concentration. The cost of L-Met for storing 100 kg CH_4 hydrate is $9.37, which is around 33.36% lower than that using L-Trp (see Table S6). In addition, its intrinsically environmentally friendly nature further strengthens its sustainability for large-scale application compared with conventional SDS.

4. Conclusion

This study proposes an environmentally benign approach for effective and ultra-rapid solidified natural gas storage by introducing L-Met modified active ice. The optimal 0.3 wt% L-Met modified active ice achieved a record-high growth rate with a t_{90} of only 3.33 min and a high CH_4 uptake of 156.05 V_g/V_w. Cryogenic scanning electron microscopy (Cryo-SEM) first confirms the loose and interconnected porous structure of active ice with open pore size ranging from 7 to 17 μm, facilitating CH_4 diffusion. *In situ* Raman spectra were used to examine the micro-kinetics of the ultra-rapid CH_4 hydrate formation process and reveal that the ultra-rapid CH_4 hydrate formation kinetics achieved is closely associated with the partially ordered hydrogen bond network induced by the 0.3 wt% L-Met modified active ice. The enhanced CH_4 hydrate formation kinetics achieved through tuning hydrogen bond ordering in active ice points to a promising direction for future SNG technology development. Furthermore, this approach establishes a green and energy-efficient pathway that avoids the environmental concerns of conventional surfactant-based CH_4 hydrate promoters. Future work will expand the active ice method through examining a series of hydrophobic amino acids with a focus on their ability to tune the favourable hydrogen bond ordering for subsequent CH_4 hydrate formation kinetics enhancement. Additionally, a continuous production process shall be developed to evaluate the economic viability and potential for large-scale SNG applications using this green and effective active ice method.

Author contributions

Y. Li: conceptualization, formal analysis, data curation, and writing – original draft. J. Zhang: investigation and formal analysis. J. Gao: investigation and funding acquisition. G. Cheng: methodology and supervision. Z. Yin: conceptualiz-

ation, methodology, formal analysis, writing – review and editing, supervision, and funding acquisition.

Conflicts of interest

There are no conflicts of interest to declare.

Abbreviations

$C_{\text{L-Met}}$	L-Methionine dosage concentration (wt%)
Cryo-SEM	Cryogenic scanning electron microscopy
DA	Single donor–single acceptor hydrogen bonds
DDAA	Double donor–double acceptor hydrogen bonds
EDS	Energy dispersive spectroscopy
FT-IR	Fourier transform infrared
$I_{\text{DDAA/DA}}$	Raman intensity of double donor–double acceptor hydrogen bonds to single donor–single acceptor hydrogen bonds
$I_{\text{S/W}}$	Infrared spectroscopy intensity of strong hydrogen bond peak to the weak hydrogen bond peak
L-Met	L-Methionine
n_g	Normalized CH_4 uptake (V_g/V_w)
N_h	Hydration number
P	Pressure (MPa)
SNG	Solidified natural gas
T	Temperature (K)
t_{ind}	Induction time (min)
t_{90}	Time required to achieve 90% final CH_4 uptake (min)
θ_L	Cage occupancy of CH_4 in $5^{12}6^2$ large cages
θ_S	Cage occupancy of CH_4 in 5^{12} small cages
C_w	Final conversion rate of water to CH_4 hydrate

Data availability

The data supporting this article are included as part of the supplementary information (SI). Supplementary information: Movies SV1, SV2, and SV3. See DOI: https://doi.org/10.1039/d5gc06216k.

Acknowledgements

The National Natural Science Foundation of China (52561145239), the GuangDong Basic and Applied Basic Research Foundation Offshore Wind Power Key Project (2023B1515250009), and the Shenzhen Science and Technology Committee (GJHZ20240218113559007 and JCYJ20250604180259061) are acknowledged. Z. Yin appreciates the financial support from the GuangDong Pearl River Talents Program (2021QN02H836) and the Shenzhen Key Laboratory of Advanced Technology for Marine Ecology (ZDSYS20230626091459009).

References

1 C. Kemfert, F. Präger, I. Braunger, F. M. Hoffart and H. Brauers, *Nat. Energy*, 2022, **7**, 582–587.
2 Y. Gan, H. M. El-Houjeiri, A. Badahdah, Z. Lu, H. Cai, S. Przesmitzki and M. Wang, *Nat. Commun.*, 2020, **11**, 824.
3 G. Lopez, D. Keiner, M. Fasihi, T. Koiranen and C. Breyer, *Energy Environ. Sci.*, 2023, **16**, 2879–2909.
4 L. Chen, G. Msigwa, M. Yang, A. I. Osman, S. Fawzy, D. W. Rooney and P.-S. Yap, *Environ. Chem. Lett.*, 2022, **20**, 2277–2310.
5 J. Zhang, Z. Yin, S. A. Khan, S. Li, Q. Li, X. Liu and P. Linga, *Lab Chip*, 2024, **24**, 1602–1615.
6 H. Tan, Q. Zhao, N. Sun and Y. Li, *Energy Convers. Manage.*, 2016, **126**, 875–888.
7 N. Armaroli and V. Balzani, *Angew. Chem., Int. Ed.*, 2007, **46**, 52–66.
8 M. I. Khan, T. Yasmin and A. Shakoor, *Renewable Sustainable Energy Rev.*, 2015, **51**, 785–797.
9 Y. Li, J. Xue, J. Peppers, N. Y. Kado, C. F. A. Vogel, C. P. Alaimo, P. G. Green, R. Zhang, B. M. Jenkins, M. Kim, T. M. Young and M. J. Kleeman, *Environ. Sci. Technol.*, 2021, **55**, 2820–2830.
10 J. D. Evans, V. Bon, I. Senkovska, H.-C. Lee and S. Kaskel, *Nat. Commun.*, 2020, **11**, 2690.
11 K. Nath, K. R. Wright, A. Ahmed, D. J. Siegel and A. J. Matzger, *J. Am. Chem. Soc.*, 2024, **146**, 10517–10523.
12 G. Bhattacharjee, M. N. Goh, S. E. K. Arumuganainar and Y. Zhang, *Energy Environ. Sci.*, 2020, **13**, 4946–4961.
13 A. Farhadian, A. Phan, Z. T. Rizi, A. Shaabani, E. Sadeh, M. Mohammad-Taheri, M. A. Aminolroayaei, A. Mohammadi, N. Sayyari and F. Wang, *Green Chem.*, 2025, **27**, 4523–4539.
14 J. Sun, Y. Zhang, G. Bhattacharjee, X. Li, L. Jiang and P. Linga, *Appl. Energy*, 2024, **368**, 123517.
15 E. Sadeh, A. Farhadian, M. Maddah, M. E. Semenov, E. R. Son, A. Heydari, U. Zh. Mirzakimov, L. R. Valiullin and M. A. Varfolomeev, *Appl. Energy*, 2025, **379**, 124924.
16 B. Mahant, O. S. Kushwaha and R. Kumar, *Energy Convers. Manage.*, 2022, **269**, 116044.
17 W. Lee, K. Kim, J. Lee, Y.-H. Ahn and J. W. Lee, *Green Chem.*, 2024, **26**, 7552–7578.
18 F. Rossi, M. Filipponi and B. Castellani, *Appl. Energy*, 2012, **99**, 167–172.
19 J. Farrando-Perez, R. Balderas-Xicohtencatl, Y. Cheng, L. Daemen, C. Cuadrado-Collados, M. Martinez-Escandell, A. J. Ramirez-Cuesta and J. Silvestre-Albero, *Nat. Commun.*, 2022, **13**, 5953.
20 P. Wang, Y. Li, N. Sun, S. Han, X. Wang, Q. Su, Y. Li, J. He, X. Yu, S. Du, J. S. Francisco, J. Zhu and Y. Zhao, *Chem. Rev.*, 2024, **124**, 10363–10385.
21 J. S. Pandey, J. L. Hansen and N. Von Solms, *Chem. Eng. J.*, 2022, **432**, 134295.
22 A. Hassanpouryouzband, E. Joonaki, M. V. Farahani, S. Takeya, C. Ruppel, J. Yang, N. J. English, J. M. Schicks, K. Edlmann, H. Mehrabian, Z. M. Aman and B. Tohidi, *Chem. Soc. Rev.*, 2020, **49**, 5225.

23 G. Bhattacharjee, N. Choudhary, A. Kumar, S. Chakrabarty and R. Kumar, *J. Nat. Gas Sci. Eng.*, 2016, **35**, 1453–1462.
24 H. Zhang, J. Zhang, L. Shang, Z. Liu, J. Chen and S. Liang, *J. Environ. Chem. Eng.*, 2025, **13**, 118882.
25 Y. Qin, L. Shang, Z. Lv, Z. Liu, J. He, X. Li, M. Binama, L. Yang and D. Wang, *Energy*, 2022, **254**, 124214.
26 E. Sadeh, A. Farhadian, M. Maddah, M. E. Semenov, E. R. Son, A. Heydari, U. Zh. Mirzakimov, L. R. Valiullin and M. A. Varfolomeev, *Appl. Energy*, 2025, **379**, 124924.
27 P. Xiao, J.-J. Li, W. Chen, W.-X. Pang, X.-W. Peng, Y. Xie, X.-H. Wang, C. Deng, C.-Y. Sun, B. Liu, Y.-J. Zhu, Y.-L. Peng, P. Linga and G.-J. Chen, *Nat. Commun.*, 2023, **14**, 8068.
28 Y. Zhang, Y. Ma, K. Jeenmuang, G. Vishwakarma, C.-Y. Sun, G.-J. Chen and P. Linga, *Nat. Commun.*, 2025, **16**, 8670.
29 J. Ren, X. Liu, M. Niu and Z. Yin, *Chem. Eng. J.*, 2022, **437**, 135368.
30 M. E. Casco, J. Silvestre-Albero, A. J. Ramírez-Cuesta, F. Rey, J. L. Jordá, A. Bansode, A. Urakawa, I. Peral, M. Martínez-Escandell, K. Kaneko and F. Rodríguez-Reinoso, *Nat. Commun.*, 2015, **6**, 6432.
31 X. Liu, J. Ren, D. Chen and Z. Yin, *Chem. Eng. J.*, 2022, **438**, 135504.
32 X. Shen, Y. Li, Y. Li, L. Shen, N. Maeda, Y. Zhang, H. Wang and X. Wang, *ACS Sustainable Chem. Eng.*, 2023, **11**, 8774–8785.
33 J. Ren, Z. Yin, G. Chen, H. Lu, C. Xu, S. Zeng, Y. Liu and P. Linga, *Chem. Eng. J.*, 2024, **488**, 151148.
34 J. Li, W. Zhao, P. Xiao, H. Zhang, K. Liu, M. Qi, B. Yang, G. Chen and C. Sun, *Chem. Eng. Sci.*, 2025, **305**, 121200.
35 H. S. Truong-Lam, S. J. Cho and J. D. Lee, *Appl. Energy*, 2019, **255**, 113834.
36 K.-F. Yan, J.-Y. Zhao, H. Chen, X.-S. Li, C.-G. Xu, Z.-Y. Chen, Y. Zhang, Y. Wang, J.-C. Feng and Y.-S. Yu, *Chem. Eng. Sci.*, 2023, **276**, 118829.
37 J. Sun, X. Liu, C. Xu, P. Bian and Z. Yin, *Chem. Eng. J.*, 2025, **521**, 166697.
38 H. S. Truong-Lam, S. J. Cho and J. D. Lee, *Appl. Energy*, 2019, **255**, 113834.
39 A. K. Sum, R. C. Burruss and E. D. Sloan, *J. Phys. Chem. B*, 1997, **101**, 7371–7377.